Large eddy simulations of reacting shock-bubble interaction

By Sidharth GS† and Graham V. Candler

Aerospace Engineering and Mechanics, University of Minnesota

Reacting shock bubble interaction, in which a combustible spherical density inhomogeneity is ignited by a shock, embodies complex variable-density fluid dynamics similar to the regime encountered in high speed propulsion. Vorticity generation and scale interaction in such flows is significantly influenced by variable-density effects. To account for these effects at subgrid-scales (SGS), we simulate reacting shock bubble interaction with a new set of Reynolds-filtered LES equations. The SGS terms in the new equations have only double correlations and do not contain time derivatives. The contribution of SGS mass flux, pressure-gradient acceleration,and velocity-dilatation appears explicitly and not implicitly within third and high order correlation SGS terms. A combination of Vreman eddy viscosity model and gradient model is used to close the equations for the simulation. The setup corresponds to the experiments of Haehn *et al*. (2012). A high strength incident shock case is considered which involves detonation of the $H_2/O_2/Xe$ gas mixture inside the bubble. The effect of combustion on the interaction is captured adequately in comparison with the experiment. Under the experimental conditions, the ignition spot is close to the downstream pole of the bubble. But it is found that higher bubble temperature can lead to ignition on the upstream pole leading to a completely different dynamics.

1. Introduction

Shock-bubble interaction [1] involves impulsive acceleration of a spherical density inhomogeneity by a planar shock wave. The shock wave compresses the bubble, and the vorticity deposited by baroclinic torque results in development of a primary vortex ring followed by formation of secondary and near-turbulent flow structures at late time depending on the strength of the interaction. Acoustic impedance (product of density and sound speed) mismatch between the bubble and the ambient gas leads to non-linear acoustic effects during shock transmission. If the bubble acoustic impedance is higher than the ambient, the shock refraction pattern is convergent and leads to focusing of the transmitted shock onto the downstream pole. Shock focusing is associated with increase in pressure and temperature and can ignite a combustible gas mixture inside the bubble.

Shock-bubble interaction in reactive gases has been studied earlier mostly in the context of shock-flame interaction [2,3]. Vorticity deposition by the shock results in enhanced mixing and combustion, followed by complex chemi-acoustic interactions. These interactions sustain turbulent reaction zones which can cause deflagration to detonation transition (DDT) in their vicinity [4]. Recently, experiments on reacting shock bubble interaction have been conducted by Haehn *et al.* [5] in the Wisconsin Shock-Tube Laboratory. The experiments demonstrated shock-initiated combustion of a H_2,O_2,Xe gas

mixture inside a heavy spherical bubble surrounded by lighter N_2 gas. Shock-focusing due to the bubble creates a hot spot, thus igniting the mixture. A range of incident shock strengths were considered in the experiment and it was found that two different regimes exist. For low shock strengths $M \lesssim 2$, ignition is weak and the reaction proceeds slowly. For high shock strengths $M \gtrsim 2.5$, combustion is rapid, volumetric and can initiate even before the completion of shock-focusing.

Extensive two-dimensional computational studies by Diegelmann *et al* [6, 7] confirm the two regimes reported in the experiments. The computations find that ignition with weak shocks $2.0 \leq M \leq 2.3$ induces a subsonic deflagration wave, while strong shocks $M > 2.3$ lead to a supersonic detonation wave. For intermediate shock strength $M = 2.19$, the simulation exhibits DDT. The authors find that for a constant shock strength, increase in ambient pressure can change the reaction wave from deflagration to detonation. The influence of the chemical reactions on the flow-field depends on the regime. They note that the dynamics of the detonated bubble differs significantly from an inert interaction, while the effect on the flow-field from deflagration combustion is weak.

Diegelmann *et al* [8] have also carried out a three-dimensional simulation of reacting shock bubble interaction (RSBI). The detonation case with $M = 2.83$ incident shock was considered. Azimuthal flow structures such as fine vortex filaments and Widnall-type instabilities [9] were observed on the axisymmetric vortex rings. The simulations slightly underpredicted the transverse bubble diameter post-detonation in comparison to the experiment. This was attributed to its sensitivity to the uncertainty in the location of ignition spot.

In this report, we present results from large eddy simulations (LES) of RSBI in the detonation regime. LES enables low-resolution but stable computations of the shock-bubble interaction. The subgrid-scale (SGS) models account for the effect of unresolved small scales and are active during the initial interfacial roll-up and later in the primary vortex ring, the upstream secondary vortex ring [10] and the downstream supersonic vortex ring [11] regions . The flow field involves strong density variations due to shocks, combustion and turbulent mixing of inhomogeneous gases. Therefore, variable-density subgrid-scale terms require modeling. We solve Reynolds-filtered LES equations to compute filtered velocity, as opposed to Favre-filtered LES equations which compute the density-weighted filtered velocity. A new set of LES equations derived in Sidharth *et al.* [12] are used. Unlike the conventional Reynolds-filtered framework, the SGS terms in these equations do not involve time derivatives or third/fourth order correlations. Also, the effect of SGS mass flux, SGS dilatation and SGS pressure-gradient acceleration can be explicitly represented.

The objective of this work is two-fold: 1) to test the new LES equations on a complex yet canonical problem that involves compressible variable-density turbulence and 2) to understand the role of ignition spot location on intermediate time RSBI dynamics. We will see that within the detonation regime, for the same bubble gas mixture composition and the incident shock Mach number, depending on the bubble temperature, the detonation wave can originate either at the upstream pole or at the refracted-shock/bubble-interface point during shock-focusing. This can lead to significantly different flow and mixing dynamics.

2. Reynolds-filtered LES equations

Let us review the formalism for filtering the Navier-Stokes equations A spatial linear filter for a flow-realization with $\mathbf{x} = x_i$ may be defined as

$$\overline{f(\mathbf{x})} = \int G_{\Delta_x}(\mathbf{x} - \mathbf{x}') f(\mathbf{x}') d^3\mathbf{x}' \tag{2.1}$$

where G_{Δ_x} is the normalized convolution kernel with an associated filter length scale Δ_x. For the continuous LES equations, we consider a homogeneous continuous filter which is independent of the implicit filter associated with the discrete solution field and the discrete differential operators. The governing equations for filtered mass, momentum, and energy are obtained from the filtered Navier-Stokes equations and written in the Reynolds-filtered form as

$$\begin{aligned} \frac{\partial}{\partial t}\begin{pmatrix} \bar{\rho} \\ \bar{\rho}\bar{u}_i + \mathcal{M}_i \\ \bar{E}_{\rm int} + \frac{1}{2}\bar{\rho}\bar{u}_k\bar{u}_k + \frac{1}{2}\tau^{\rm R}_{kk} \end{pmatrix} + \frac{\partial}{\partial x_j}\begin{pmatrix} \bar{\rho}\bar{u}_j \\ \bar{\rho}\bar{u}_i\bar{u}_j + \bar{p}\delta_{ij} \\ \frac{1}{2}\bar{\rho}\bar{u}_k\bar{u}_k\bar{u}_j + \bar{E}_{\rm int}\bar{u}_j + \bar{p}\bar{u}_j \end{pmatrix} \\ + \frac{\partial}{\partial x_j}\begin{pmatrix} \mathcal{M}_j \\ \tau^{\rm R}_{ij} \\ \mathcal{K}^{\rm R}_j + \mathcal{H}^{\rm R}_j \end{pmatrix} = \begin{pmatrix} 0 \\ \bar{\sigma}_{\rho u_i} \\ \bar{\sigma}_E \end{pmatrix} \end{aligned} \tag{2.2}$$

$E_{\rm int}$ represents the internal energy per unit volume. The terms $\sigma_{\rho u_i}$ and σ_E correspond to diffusive molecular transport in the momentum and the energy equations,s respectively. In the present analysis, the resolved-scale and the SGS terms that arise from the expressions from $\bar{\sigma}_{\rho u_i}$ and $\bar{\sigma}_E$ are not expanded. The superscript 'R' denotes the use of Reynolds-filtered velocity $\bar{u}_i$. Here,

$$\begin{aligned} &\mathcal{M}_i = \overline{\rho u_i} - \bar{\rho}\bar{u}_i, \;\; \tau^{\rm R}_{ij} = \overline{\rho u_i u_j} - \bar{\rho}\bar{u}_i\bar{u}_j \\ &\mathcal{K}^{\rm R}_j = \overline{\rho u_k u_k u_j} - \bar{\rho}\bar{u}_k\bar{u}_k\bar{u}_j, \;\; \mathcal{H}^{\rm R}_j = \overline{(E_{\rm int} + p)u_j} - (\bar{E}_{\rm int} + \bar{p})\bar{u}_j \end{aligned} \tag{2.3}$$

$\mathcal{M}_i$ is the SGS mass flux. The transport equations for $\tilde{u}_i = \overline{\rho u_i}/\bar{\rho}$ and $\bar{u}_i$ can be used to derive the inviscid transport equation for $\mathcal{M}_i$.

$$\frac{\partial(\overline{\rho u_i} - \bar{\rho}\bar{u}_i)}{\partial t} = -\frac{\partial \overline{\rho u_i u_j}}{\partial x_j} + \bar{u}_i\frac{\partial \mathcal{M}_j}{\partial x_j} + \frac{\partial \bar{\rho}\bar{u}_i\bar{u}_j}{\partial x_j} + \bar{\rho}\frac{\partial \mathcal{T}[u_i, u_j]}{\partial x_j} - \bar{\rho}\mathcal{T}[u_i, \frac{\partial u_j}{\partial x_j}] - \mathcal{T}[\rho, \frac{1}{\rho}\frac{\partial p}{\partial x_i}] \tag{2.4}$$

For the sake of clarity, we do not consider terms corresponding to viscous molecular transport; including viscous transport term is straight-forward and produces an additional term, $\mathcal{T}[\rho, \sigma_{\rho u_i}/\rho]$. Substituting for $\partial_t \mathcal{M}_i$ and $\partial_t \tau^{\rm R}_{kk}/2$ we can write the Reynolds-filtered LES equations as:

$$\frac{\partial}{\partial x_j}\begin{pmatrix} \bar{\rho} \\ \bar{\rho}\bar{u}_i \\ \bar{E}_{\rm int} + \frac{1}{2}\bar{\rho}\bar{u}_k\bar{u}_k \end{pmatrix} + \frac{\partial}{\partial x_j}\begin{pmatrix} \bar{\rho}\bar{u}_j \\ \bar{\rho}\bar{u}_i\bar{u}_j + \bar{p}\delta_{ij} \\ \frac{1}{2}\bar{\rho}\bar{u}_k\bar{u}_k\bar{u}_j + \bar{E}_{\rm int}\bar{u}_j + \bar{p}\bar{u}_j \end{pmatrix} + \begin{pmatrix} \mathcal{S}_\rho \\ \mathcal{S}_{\rho u_i} \\ \mathcal{S}_E \end{pmatrix} = \begin{pmatrix} 0 \\ \bar{\sigma}_{\rho u_i} \\ \bar{\sigma}_E \end{pmatrix} \tag{2.5}$$

where the SGS contribution to the governing equations is:

$$\mathcal{S}_\rho = \frac{\partial \mathcal{T}[\rho, u_j]}{\partial x_j} \tag{2.6}$$

$$\mathcal{S}_{\rho u_i} = \bar{u}_i \mathcal{S}_\rho + \bar{\rho}\frac{\partial \mathcal{T}[u_i, u_j]}{\partial x_j} - \mathcal{T}[\rho, \frac{1}{\rho}\frac{\partial p}{\partial x_i}] - \bar{\rho}\,\mathcal{T}[\nabla \cdot u, u_i] \tag{2.7}$$

$$\mathcal{S}_E = \bar{u}_i \mathcal{S}_{\rho u_i} - \frac{1}{2}\bar{u}_i\bar{u}_i\mathcal{S}_\rho + \frac{\partial \mathcal{T}[E_{\text{int}}, u_j]}{\partial x_j} + \mathcal{T}[\nabla \cdot u, p] \tag{2.8}$$

We use the notation $\mathcal{T}[a, b] = \overline{ab} - \bar{a}\bar{b}$ to denote central moments under the filter operator for any two physical variables a and b. The conservation-law form of the closed convective terms is maintained and the non-conservative SGS source terms arise as a consequence of choosing to solve for the filtered velocity instead of the filtered momentum. The SGS terms that are unclosed and need to be modeled in this formulation are:

- SGS mass flux $\mathcal{T}[\rho, u_i] = \overline{\rho u_i} - \bar{\rho}\bar{u}_i$
- SGS specific stress $\mathcal{T}[u_i, u_j] = \overline{u_i u_j} - \bar{u}_i\bar{u}_j$
- SGS dilatational flux $\mathcal{T}[\nabla \cdot u, u_i] = \overline{(\nabla \cdot u)u_i} - (\nabla \cdot \bar{u})\bar{u}_i$
- SGS pressure work $\mathcal{T}[\nabla \cdot u, p] = \overline{(\nabla \cdot u)p} - (\nabla \cdot \bar{u})\bar{p}$
- SGS pressure acceleration $\mathcal{T}[\rho, \nabla_i p/\rho]/\bar{\rho} = -(\overline{\nabla_i p/\rho} - \nabla_i \bar{p}/\bar{\rho})$
- SGS internal energy flux $\mathcal{T}[E_{\text{int}}, u_i] = \overline{E_{\text{int}} u_i} - \bar{E}_{\text{int}}\bar{u}_i$

For multicomponent reacting flows, the density of each gas species ρ_s is transported. Therefore, we consider the filtered scalar advection equation with diffusion and source terms. The transport equation for the filtered scalar $\bar{c}$ can be derived and expressed in a conservation law form as under:

$$\frac{\partial \bar{\rho}\bar{c}}{\partial t} + \frac{\partial \bar{\rho}\bar{u}_j\bar{c}}{\partial x_j} + \mathcal{S}_{\rho c} = \bar{\rho}\bar{\Omega}_c + \bar{\sigma}_{\rho c}, \text{ where } \mathcal{S}_{\rho c} = \bar{\rho}\frac{\partial \mathcal{T}[c, u_j]}{\partial x_j} + \bar{c}\,\mathcal{S}_\rho - \bar{\rho}\mathcal{T}[c, \frac{\partial u_j}{\partial x_j}] \tag{2.9}$$

$\mathcal{S}_{\rho c}$ is the subgrid-scale contribution, $\sigma_{\rho c}$ is the viscous diffusion term, and Ω_c represents the source term in the transport equation of the scalar c. Equation (2.9) is obtained by decoupling the inviscid transport equation for $\mathcal{T}[\rho, c]$ from $\partial_t\overline{\rho c}$, similar to the procedure we adopt for the resolved-scale momentum and the energy equations. We observe that usage of filtered velocity does not involve the trivariate moment $\mathcal{T}[\rho, u_j, c]$. In this work, we do not consider the SGS turbulent chemical source term $\bar{\Omega} - \Omega(\bar{E}_{\text{int}}, \bar{\rho}_s)$ and assume laminar finite rate chemistry. In the detonation regime of RSBI, combustion takes place inside the bubble before turbulent structures develop. Therefore, the SGS turbulent chemical source term is expected to be negligible during the detonation phase.

2.1. *Subgrid-scale models*

We discuss the SGS models employed for closure. SGS specific stress and SGS fluxes of density, species mass fractions, internal energy are modeled with the Vreman eddy viscosity model [13]. The Vreman model has been demonstrated to perform well on transitional and turbulent shear layers. This is important for modeling of the small-scales present in SBI on the interface of the bubble after the shock transit. The eddy viscosity in Vreman model is computed as

$$\nu_e = 2.5 C_S^2 \Delta_c \sqrt{\frac{\mathbf{II}(G(u_i,u_j))}{\mathbf{I}(G(u_i,u_j))}} \quad \text{where } G(a,b) = \frac{\Delta_c^2}{12}\frac{\partial \bar{a}}{\partial x_k}\frac{\partial \bar{b}}{\partial x_k} \tag{2.10}$$

Here $G(a,b)$ for two physical quantities a and b represents the gradient model [14] closure for $\mathcal{T}[a,b] = \overline{ab} - \bar{a}\bar{b}$. C_S is the Smagorinsky coefficient. $\mathbf{I}(A_{ij})$ and $\mathbf{II}(A_{ij})$ are the first and second invariants of any tensor A_{ij}. The SGS Prandtl number and SGS Schmidt number are taken to be 0.9 and 1.0 respectively. For SGS pressure-gradient acceleration and SGS dilatation correlations, we use the gradient model closure.

$$\mathcal{T}[\rho, \partial_i p/\rho] = \partial_i \bar{p}\mathcal{T}[\rho, 1/\rho] - \bar{\rho}\mathcal{T}[\partial_i p, 1/\rho] \overset{\text{m}}{=} \partial_i \bar{p}\, G(\rho, 1/\rho) - \bar{\rho}\, G(\partial_i p, 1/\rho) \tag{2.11}$$

$$\mathcal{T}[u_i, \partial_j u_j] \overset{\text{m}}{=} G[u_i, \partial_j u_j], \;\; \mathcal{T}[p, \partial_j u_j] \overset{\text{m}}{=} G[p, \partial_j u_j] \tag{2.12}$$

We do not model the SGS mass fraction dilatation term, $\mathcal{T}[c_s, \partial_j u_j]$ in this work.

3. Numerical method and computational setup

3.1. *Numerical Methodology*

We solve the Reynolds-filtered Navier-Stokes equations (Equation 2.8) using a finite volume discretization.

$$\frac{\partial \mathrm{U}}{\partial t} + \frac{\partial \mathrm{F}_j}{\partial x_j} + \sigma + \mathcal{S} = \Omega \tag{3.1}$$

The solution vector is $\mathrm{U} = (\bar{\rho}_s, \bar{\rho}\bar{u}_i, \bar{E}_{\text{int}} + \bar{\rho}\bar{u}_k\bar{u}_k/2 + \bar{\rho}_s h_s^0)$. F_j is the resolved-scale inviscid flux and $\sigma = (\sigma_{\rho_s}, \sigma_{\rho u_i}, \sigma_E)$ is the molecular diffusion vector. $\mathcal{S}$ is the SGS vector and $\Omega = (\dot{\omega}_s, 0, 0)$ is the chemical source term vector.

The inviscid flux is evaluated using a stable low-dissipation scheme based on the 'kinetic-energy consistent' method developed by [15]. A gradient reconstruction method described in [16] is used to make the symmetric part of the convective flux formally sixth-order accurate on Cartesian grids. Local-maximum-principle-preserving limiters on ρ_s are used similar to the method outlined in [17]. Dissipation for shock-capturing and contact is added to the symmetric flux in the form of a modified Steger-Warming flux-vector splitting scheme. The details of the flux scheme can be found in [18]. The inviscid flux can be written in the form:

$$F_j = F_j^{\text{sym}} + (1/2)\alpha(\mathrm{R}^{-1}|\Lambda|\mathrm{R})(U_R - U_L) \tag{3.2}$$

U_R and U_L are second-order limited reconstructed states. R and R^{-1} are the eigenvector matrices of the inviscid flux Jacobian. α is the shock/contact detector and its values ranges from 0 to 1. Typically, a shock sensor such as the Ducros switch [19] is used to localize dissipation at the shocks in a vortically dominated flow. But for flows with Richtmyer-Meshkov instabilities, the sensor is found to generate spurious small scales and break symmetry. This is attributed to the switch field being highly intermittent in space and time. Intermittent dissipation field generates small-scale vorticity and disturbance waves which further sporadically activate the switch. This feedback loop results in self-sustained error generation, which shows its imprints at late time statistics. In this work, we use a spatially constant value of $\alpha = 0.3$, which reduces gradually with time to $\alpha = 0.1$ after the shock wave transits the bubble and detonation is complete. This

results in high values of numerical dissipation in the entire domain, but is conservative on dispersion error generated in the simulation.

The molecular diffusion terms are computed using a second-order central scheme and use compact stencil second-order least-squares gradients. Viscosity is computed using Blottner fits and Wilke's mixing rule. For mass diffusion, we use an approximation by using a constant diffusion coefficient $\sigma_{\rho_s} = \partial_j(\bar{\rho} D \partial_j Y_s)$. Y_s is the mass fraction of species s and D is the diffusion coefficient obtained using constant Lewis number of 1.0. Ideally, a species diffusion coefficient matrix $D_{s1,s2}$ must be used as it is more accurate but the effect of accurate mass diffusion models on RSBI is not addressed in this work.

The chemical source term for species densities, $\dot{\omega}_s$ is evaluated as

$$\dot{\omega}_s = M_s \sum_{r=1}^{N_r} (\nu_{sr}^b - \nu_{sr}^f) \Gamma_s \Big(k_r^f \prod_{s'=1}^{N_s} [X_{s'}]^{\nu_{s'r}^f} - k_r^b \prod_{s'=1}^{N_s} [X_{s'}]^{\nu_{s'r}^b} \Big) \tag{3.3}$$

$[X_s]$ is the molar concentration of species s, M_s is its molecular weight. ν_{sr}^f, ν_{sr}^b is the molar stoichiometric coefficients of the forward/backward reaction for species s and reaction r. k_r^f, k_r^b are the reaction rates of reaction r. Γ_r is the third body efficiency of reaction r. The reaction rates are computed in the Arrhenius form with the reaction rate $k^f = AT^\eta \exp(-E_a/RT)$ where E_a is the activation energy, A is the pre-exponential factor, and η is the temperature exponent. All parameters are reaction specific. k^b is computed from the equilibrium constant of the reaction.

For temporal discretization, we employ the Strang time splitting to account for stiff chemistry.

$$\frac{\partial \mathrm{U}}{\partial t} = -\Big(\frac{\partial \mathrm{F}_j}{\partial x_j} + \sigma + \mathcal{S} \Big) + \Omega \tag{3.4}$$

Ω vector is integrated using fourth order accurate semi-implicit GRK4A [20], while all other terms are integrated using the third order accurate SSPRK3 [21].

The reaction system in the simulation is hydrogen combustion. We are interested in the fast ignition regime that occurs above the 'crossover' temperature ($\sim$950K at 1 atm). In this regime, ignition occurs via chain branching explosion initiated by formation of HO_2 and H radicals. We model detailed chemical kinetics using Hong *et al* mechanism [22] with 8 species and 20 reactions. The 20 reactions may be grouped into four broad categories: hydrogen-oxygen shuffle reactions, hydroperoxyl reactions, radical-radical recombination reactions, and hydrogen-peroxide reactions. The mechanism provides improved rate constants for OH and HO_2 product reactions at high temperatures and has been shown to perform reliably at $T >$ 3000K. The third body efficiency of Xe is set to be the same as that of Ar. We do not include the high pressure limit (Troe fall-off parameters) as the case considered in this work does not involves local pressures high enough to cause significant departures from the low-pressure limit parameters of the mechanism. In detonation, the induction time-scales are comparable or shorter than vibrational relaxation time scales for the shock leading the detonation. Therefore, vibrational relaxation effects can be important for accurate computation of thermochemical state and wave propagation velocities. However, for simplicity, we do not model vibrational relaxation of the species in the current work.

3.2. *Computational setup*

The computational setup based on the experiment [5] is shown in figure 1. A shock at Mach number of 2.83 is incident on a shock bubble with radius $r = 0.02$m in a frame of

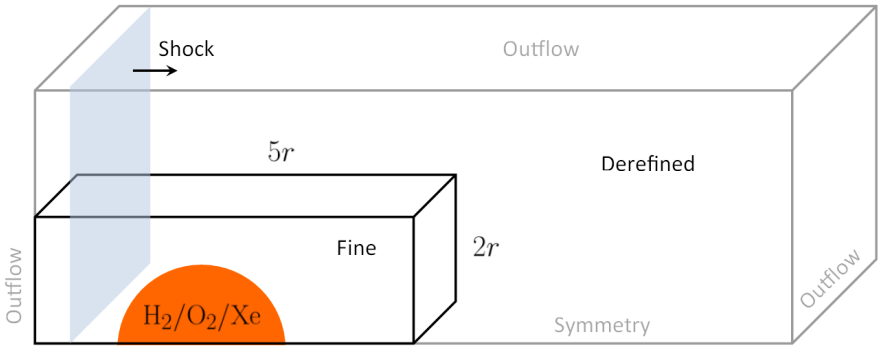

FIGURE 1. Computational setup for the shock-bubble interaction simulations

reference moving with 200m/s. Only a quarter of the bubble is simulated. The refined region of the domain is $5r \times 2r \times 2r$ with $r/\Delta = 80$. As seen from the figure, there is no derefined region upstream of the bubble. While this works well with upstream traveling shock waves, it is not effective for weak acoustic waves. However, since the numerical dissipation at the interface in the current simulations is high, this does not have a considerable effect on the interface development. The bubble gas mixture has a molar composition of H_2:O_2:Xe=1:2:3.75. The ambient gas is N_2. The density of the bubble is 3.28 kg/m^3. The Atwood number for the bubble corresponds to 0.5. The pre-shocked pressure p_0 and temperature T_0 are 1 atm and 295K respectively. The hydrodynamic time-scale based on shock-traversal time is 40 µs. We also simulate a case where the pres-shocked p_0, T_0 are higher by a factor of 1.25. It will be seen in the next subsection that this changes the location of the ignition spot from downstream hemisphere to upstream pole, leading to a different kind of dynamics.

3.3. *2D high resolution simulations*

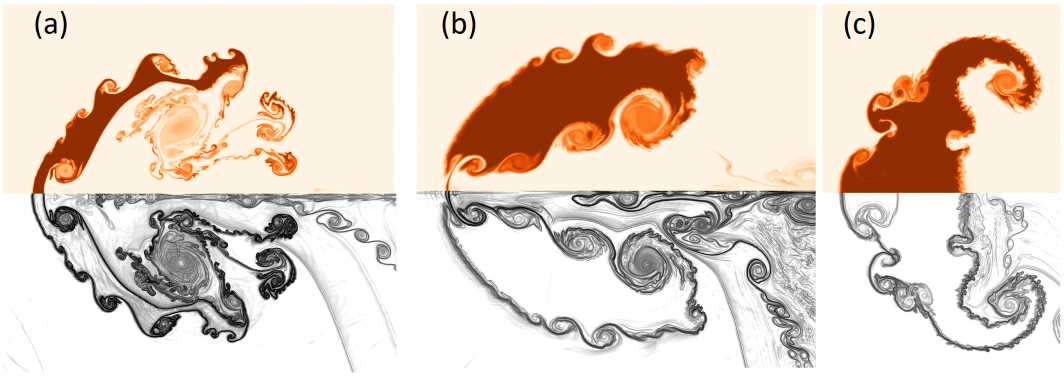

FIGURE 2. High resolution 2D simulations: Mass fraction of Xe (top) and log$|\nabla\rho|$ (bottom) at inermediate time t=240 µs for (a) inert, (b) reacting case (p_0 = 1 atm) and (c) reacting case (p_0 = 1.25 atm)

We carry out high resolution two-dimensional simulations as a preliminary exercise to understand the flow characteristics, time scales and sequence of events in the inert and reacting cases. An intermediate time snapshot of the flow-field is shown in figure 2. Case (a) is the inert case, while cases (b) and (c) correspond to the reacting cases. The

difference between cases (b) and (c) is that ambient pressure and temperature is higher. In case (b), detonation occurs at the refracted shock/interface point during shock transit. This results in detonation right when the incident shock hits the bubble. It is important to note that it is the increase in initial bubble temperature at this composition and shock Mach number that shifts the ignition spot. This was independently confirmed by keeping the ambient pressure at p_0 and increasing the bubble temperature.

Detailed evolution of the interaction including the detonation wave is visualized in [6,7]. Dynamics in case (c) here resembles the $M = 2.9$ condition considered in [7]. It is seen that the interface development in case (c) is Richtmyer-Meshkov/Rayleigh-Taylor type while primary interface instability in case (b) is Kelvin-Helmholtz type. In general, the primary difference between inert and reacting cases is the reduced mixing between bubble and ambient fluid in the reacting cases. Unlike the inert case which has two main vortices, case (b) has multiple vortices on the lower interface.

The case (b) flow-field is explicitly filtered to estimate the importance of variable-density SGS terms in the Reynolds-filtered momentum equation. Using an exponential filter with filter $\Delta_c = 5\Delta$, we compute the magnitude of the individual SGS terms in $\mathcal{S}_{\rho u_i}$ and plot them in figure 3. It is seen that variable-density SGS terms (ii-iv) are active and non-negligible. Although this is a two-dimensional flow-field, it is expected that the terms will actively contribute in 3D LES where the models are active in an *a posteriori* sense.

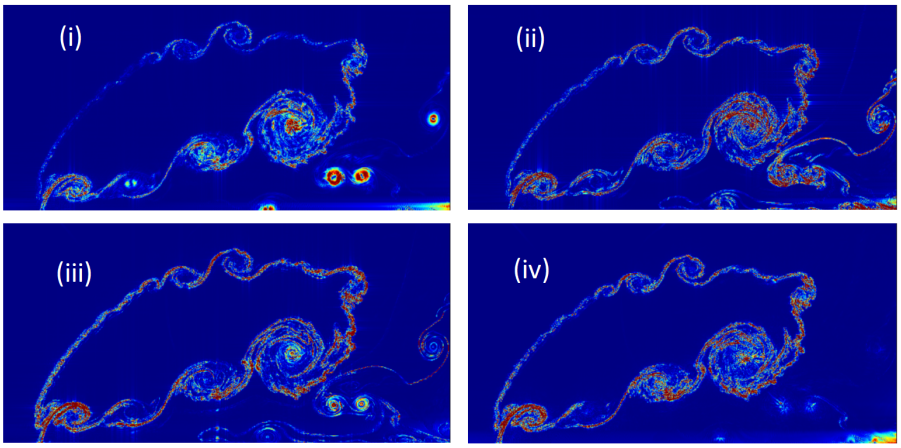

FIGURE 3. *A priori* estimate of magnitude of SGS terms in the Reynolds-filtered momentum equation for case (b): (i) SGS specific stress term, (ii) SGS mass flux convection, (iii) SGS pressure-gradient acceleration term, and (iv) SGS velocity dilatation term. An exponential filter with $\Delta_c = 5\Delta$ is used. All quantities are plotted on the same scale.

4. Large eddy simulation results

The results from large eddy simulations from the inert (case a) and reacting (cases b and c) interactions are presented in this section. Case (c) is simulated to study the dynamics with higher bubble temperature. However, to keep the Atwood number of the interaction fixed, the initial temperature of both the bubble and the ambient is increased to 372K.

Similar to the two-dimensional results, the spatio-temporal evolution of the reacting cases exhibit differences from the inert case. This is reflected not only in the bubble

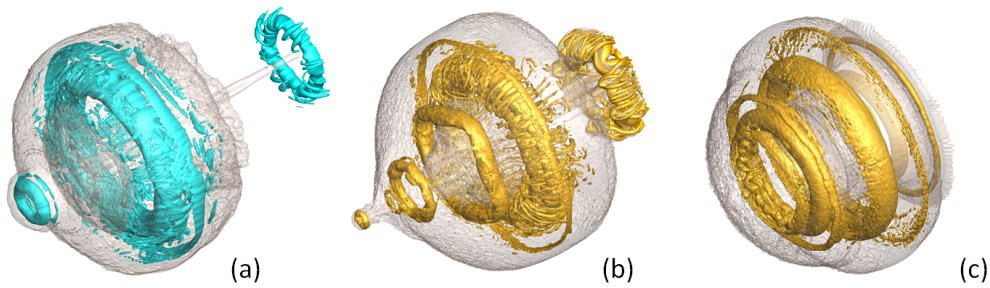

FIGURE 4. Large eddy simulation results of (a) inert, (b) reacting case T_0 and (c) reacting case $1.25T_0$: isosurfaces of Q criterion (different values for the three cases) and $Y_{\mathrm{Xe}} = 10^{-3}$ at $t^* = 5$

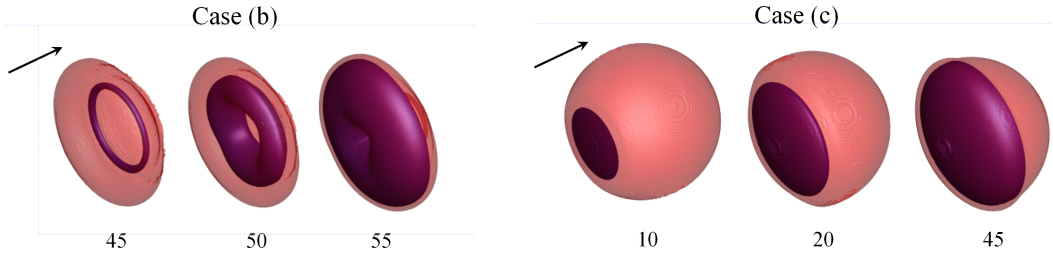

FIGURE 5. Visualization of the detonation waves inside the compressed bubble (translucent) using T isosurface values in reacting cases (b) and (c). The numbers indicate the time in µs.

size due to volumetric expansion, but also the vortex ring system development at the intermediate stage. Figure 4 visualizes the vortex structures in the flow-field at $t = 200$ µs or $t^* = 5$. The inert case has a stronger shear layer at the interface and shows the three main vortex ring systems: primary (middle), secondary (front) and the supersonic ring (rear). The primary vortex ring and its interaction with the interfacial vortex sheet results in small-scale vortex filaments. These kind of three-dimensional structures affect the ring evolution and cannot be captured by two-dimensional simulations. The reacting case (b), in contrast contains multiple vortex ring systems, albeit weaker in intensity. The primary vortex ring and the downstream rings have significant small-scale filaments. The secondary rings in the front display presence of azimuthal deformations, some of which are a consequence of symmetry boundary conditions and non-isotropic nature of the numerics. The hot bubble reacting case (c) has a different morphology from (a) and (b). The most striking difference is the absence of streamwise projectile structures in the front and the back of the bubble. The rear supersonic ring is extremely weak and does not show up in the figure. There are three large diameter rings with nearly no azimuthal small-scale filaments. Some weak three-dimensionality on the interfacial shear layer and Widnall-type instability on rings is observed.

In both reacting cases, with $M = 2.83$ incident shock, combustion takes place before vortex ring development. This is seen in the figure 5. The origin of detonation wave can be seen to shift from downstream hemisphere (case b) to upstream pole (case c) with higher initial bubble temperature. We also visualize the profiles of hydroperoxyl and hydrogen radicals across the detonation wave (figure 6). Qualitatively, the trends of radical profiles are similar to those observed in a Chapman-Jouguet detonation in

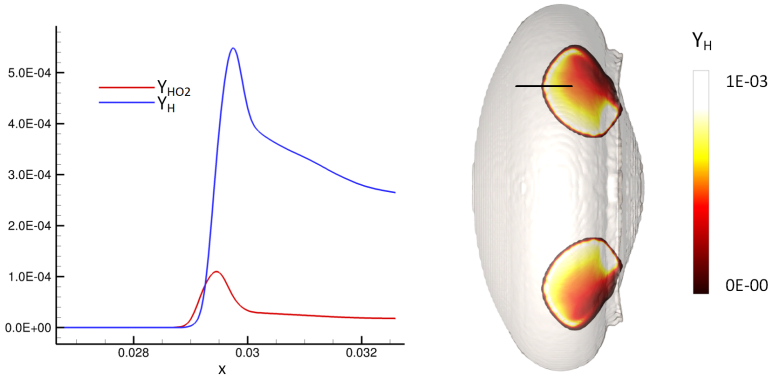

FIGURE 6. Mass fraction profiles of H and HO2 across the detonation wave in case (b) at t=50 µs.

stoichiometric H_2/Air [23] except the peak in mass fraction profile of H is much higher than that of HO2.

The evolution of the transverse bubble width (TW) is compared with the experiment in figure 7. Case (b) corresponds to the experimental conditions. Although the expansion rate in the post-detonation phase is captured correctly, the peak TW values are under-predicted similar to the high resolution 3D simulations in [8]. This can be attributed to the experimental uncertainty in the ignition spot on account of thermal/compositional fluctuations in the bubble. It is also interesting to observe that expansion rate in case (c) is much slower and the peak TW is reached at much later time. Therefore, the large scatter in the experimental data around $t^* = 6$ may potentially be explained by different ignition locations in different runs.

We also comment on the chemiluminescence images observed in the experiment. The signals from the experiment indicate presence of two bright spots inside the bubble, the explanation for which is not clear. From current simulations, we observe, in both reacting cases, two local OH maxima (figure 8). It is possible that the bright spots in OH chemiluminescence correspond to those local maxima. Since the exposure times in the experiment are long and the OH maxima are found to exist in the simulations for some time post-combustion, the hypothesis is consistent.

The activity of SGS terms in the simulation, particularly the variable-density SGS terms is of interest. In the initial phases of the interaction, the SGS terms are active only in the shear layer deposited by the shock and at the bubble poles where there are sharp gradients in the flow quantities. Later as three-dimensional instabilities and small-scale structures develop on the vortex ring systems and the center line jet (cases a and b), the SGS terms become active. To determine the size of the modeled variable-density SGS terms in comparison to the constant density SGS term in the Reynolds-filtered momentum equation, we plot the regularized ratio of the SGS vector projection on $\bar{u}_i$. This scalar metric is relevant as it represents the contribution of the SGS terms to resolved-scale kinetic energy. Figure 9 reveals that the modeled variable-density SGS terms are large and surpass the contribution of the SGS specific stress terms in certain regions in the domain. This has implications for modeling of variable-density SGS effects in LES of high speed combustion.

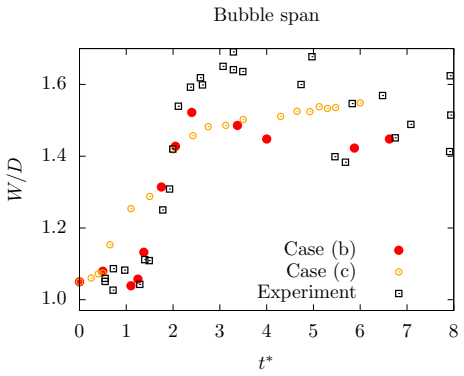

FIGURE 7. Comparison with experiment: normalized transverse bubble diameter/span as a function of non-dimensional time

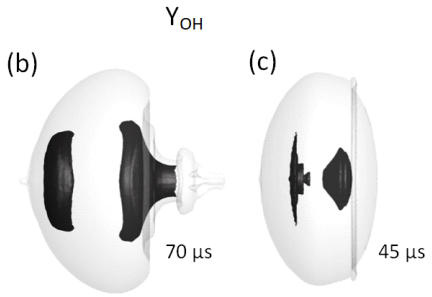

FIGURE 8. OH mass fraction isosurfaces in the two reacting cases indicate presence of two local maxima

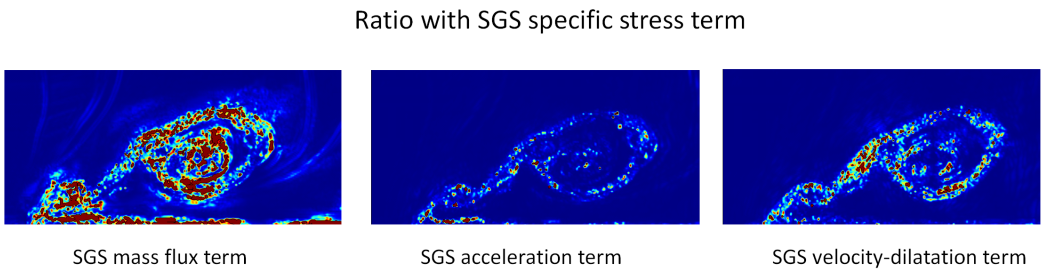

FIGURE 9. Plots of ratios of variable density SGS terms V_i in $\mathcal{S}_{\rho u_i}$ (Eqn. 2.7) with the SGS specific stress term $|V_i\bar{u}_i|/(|\bar{\rho}\bar{u}_i\partial_j\mathcal{T}[u_i,u_j]|+10^{-6})$ at $t = 240$ µs. The ratio is greater than 1 in regions bounded by black lines.

5. Conclusions and future work

The report presents results from Reynolds-filtered large eddy simulations of reacting shock-bubble interaction. A strong interaction with $M = 2.83$ incident shock is considered. The flow dynamics is complex involving baroclinic vorticity deposition, detonation, volumetric expansion, chemi-acoustic interactions and quasi-turbulent mixing. This work demonstrates that the new set of Reynolds-filtered velocity equations can simulate complex variable-density flow-dynamics. The equations takes into account the dilatational and inertial effects at subgrid-scales. In particular, the effect of SGS mass flux, SGS pressure-gradient acceleration, and SGS velocity-dilatation is explicitly modeled. This is important from the point of view of resolved-scale vorticity transport as the curl of SGS pressure-gradient acceleration is the SGS baroclinic torque.

The results from the simulation compare well with the experiment in terms of the time evolution of the transverse bubble width. In our study, we find that the ignition point of detonation can move from the downstream hemisphere to the upstream pole as the initial temperature of the bubble gas is increased. This changes the interaction dynamics significantly, resulting in a different kind of vortex ring system and transverse width evolution. Therefore, thermal fluctuation content in the bubble is an important parameter for uncertainty quantification of the RSBI analysis. In the future, high resolution simulations with accurate mass diffusion and vibrational relaxation models will help make predic-

tive quantification of the flow and the thermo-chemical state in different stages of the interaction.

Acknowledgments

This work was sponsored by Air Force Office of Scientific Research under grant numbers FA9550-12-1-0461, FA9550-17-1-0250 and Department of Energy/National Nuclear Security Administration Award number DE-NA0002382. The views and conclusions contained herein are those of the authors and should not be interpreted as necessarily representing the official policies or endorsements, either expressed or implied, of the funding agencies or the U.S. Government. Financial support has been provided by the German Research Foundation (Deutsche Forschungsgemeinschaft – DFG) in the framework of the Sonderforschungsbereich Transregio 40.

References

[1] RANJAN, D., OAKLEY, J. AND BONAZZA, R. (2011). Shock-bubble interactions. *Annual Review of Fluid Mechanics*, **43**, 117–140.

[2] THOMAS, G., BAMBREY, R. AND BROWN, C. (2001). Experimental observations of flame acceleration and transition to detonation following shock-flame interaction. *Combustion Theory and Modelling*, **5**(4), 573–594. DOI 10.1088/1364-7830/5/4/304. URL http://dx.doi.org/10.1088/1364-7830/5/4/304. http://dx.doi.org/10.1088/1364-7830/5/4/304.

[3] MARKSTEIN, G.H. (2014). *Nonsteady flame propagation: AGARDograph*, vol. 75. Elsevier.

[4] ORAN, E.S. AND GAMEZO, V.N. (2007). Origins of the deflagration-to-detonation transition in gas-phase combustion. *Combustion and Flame*, **148**(1), 4–47.

[5] HAEHN, N., RANJAN, D., WEBER, C., OAKLEY, J., ROTHAMER, D. AND BONAZZA, R. (2012). Reacting shock bubble interaction. *Combustion and Flame*, **159**(3), 1339–1350.

[6] DIEGELMANN, F., HICKEL, S. AND ADAMS, N.A. (2016). Shock mach number influence on reaction wave types and mixing in reactive shock–bubble interaction. *Combustion and Flame*, **174**, 85–99.

[7] DIEGELMANN, F., TRITSCHLER, V., HICKEL, S. AND ADAMS, N. (2016). On the pressure dependence of ignition and mixing in two-dimensional reactive shock-bubble interaction. *Combustion and Flame*, **163**, 414–426.

[8] DIEGELMANN, F., HICKEL, S. AND ADAMS, N.A. (2017). Three-dimensional reacting shock–bubble interaction. *Combustion and Flame*, **181**, 300–314.

[9] WIDNALL, S.E., BLISS, D.B. AND TSAI, C.Y. (1974). The instability of short waves on a vortex ring. *Journal of Fluid Mechanics*, **66**(1), 35–47.

[10] RANJAN, D., ANDERSON, M., OAKLEY, J. AND BONAZZA, R. (2005). Experimental investigation of a strongly shocked gas bubble. *Physical review letters*, **94**(18), 184507.

[11] WINKLER, K., CHALMERS, J.W., HODSON, S.W., WOODWARD, P.R. AND ZABUSKY, N.J. (1987). A numerical laboratory. *Physics Today*, **40**(10), 28–37.

[12] SIDHARTH, G., KARTHA, A. AND CANDLER, G.V. (2016). Filtered velocity based les of mixing in high speed recirculating shear flow. *46$^{\text{th}}$ AIAA Fluid Dynamics Conference*.

[13] VREMAN, A. (2004). An eddy-viscosity subgrid-scale model for turbulent shear flow: Algebraic theory and applications. *Physics of fluids*, **16**(10), 3670–3681.

[14] LEONARD, A. (1975). Energy cascade in large-eddy simulations of turbulent fluid flows. *Advances in geophysics*, **18**, 237–248.

[15] SUBBAREDDY, P.K. AND CANDLER, G.V. (2009). A fully discrete, kinetic energy consistent finite-volume scheme for compressible flows. *Journal of Computational Physics*, **228**(5), 1347–1364.

[16] SUBBAREDDY, P.K., BARTKOWICZ, M.D. AND CANDLER, G.V. (2014). Direct numerical simulation of high-speed transition due to an isolated roughness element. *Journal of Fluid Mechanics*, **748**, 848–878.

[17] SUBBAREDDY, P.K., KARTHA, A. AND CANDLER, G.V. (2017). Scalar conservation and boundedness in simulations of compressible flow. *Journal of Computational Physics*, **348**, 827–846.

[18] CANDLER, G.V., SUBBAREDDY, P.K. AND NOMPELIS, I. (2015). Cfd methods for hypersonic flows and aerothermodynamics. *Hypersonic Nonequilibrium Flows: Fundamentals and Recent Advances*, 203–237.

[19] DUCROS, F., FERRAND, V., NICOUD, F., WEBER, C., DARRACQ, D., GACHERIEU, C. AND POINSOT, T. (1999). Large-eddy simulation of the shock/turbulence interaction. *Journal of Computational Physics*, **152**(2), 517–549.

[20] KAPS, P. AND RENTROP, P. (1984). Application of a variable-order semi-implicit runge-kutta method to chemical models. *Computers & chemical engineering*, **8**(6), 393–396.

[21] GOTTLIEB, S., SHU, C.W. AND TADMOR, E. (2001). Strong stability-preserving high-order time discretization methods. *SIAM review*, **43**(1), 89–112.

[22] HONG, Z., DAVIDSON, D.F. AND HANSON, R.K. (2011). An improved h 2/o 2 mechanism based on recent shock tube/laser absorption measurements. *Combustion and Flame*, **158**(4), 633–644.

[23] SÁNCHEZ, A.L. AND WILLIAMS, F.A. (2014). Recent advances in understanding of flammability characteristics of hydrogen. *Progress in energy and combustion science*, **41**, 1–55.